

QUANTIFYING THE BIASES OF SPECTROSCOPICALLY SELECTED GRAVITATIONAL LENSES

RYAN A. ARNESON^{1,2}, JOEL R. BROWNSTEIN¹, ADAM S. BOLTON¹¹Department of Physics and Astronomy, University of Utah, Salt Lake City, UT 84112, USA.²Department of Physics and Astronomy, University of California at Irvine, Irvine, CA 92697, USA.

ABSTRACT

Spectroscopic selection has been the most productive technique for the selection of galaxy-scale strong gravitational lens systems with known redshifts. Statistically significant samples of strong lenses provide a powerful method for measuring the mass-density parameters of the lensing population, but results can only be generalized to the parent population if the lensing selection biases are sufficiently understood. We perform controlled Monte Carlo simulations of spectroscopic lens surveys in order to quantify the bias of lenses relative to parent galaxies in velocity dispersion, mass axis ratio, and mass density profile. For parameters typical of the SLACS and BELLS surveys, we find: (1) no significant mass axis ratio detection bias of lenses relative to parent galaxies; (2) a very small detection bias toward shallow mass density profiles, which is likely negligible compared to other sources of uncertainty in this parameter; (3) a detection bias towards smaller Einstein radius for systems drawn from parent populations with group- and cluster-scale lensing masses; and (4) a lens-modeling bias towards larger velocity dispersions for systems drawn from parent samples with sub-arcsecond mean Einstein radii. This last finding indicates that the incorporation of velocity-dispersion upper limits of *non-lenses* is an important ingredient for unbiased analyses of spectroscopically selected lens samples. In general we find that the completeness of spectroscopic lens surveys in the plane of Einstein radius and mass-density profile power-law index is quite uniform, up to a sharp drop in the region of large Einstein radius and steep mass density profile, and hence that such surveys are ideally suited to the study of massive field galaxies.

Keywords: galaxies: statistics – gravitational lensing: strong – surveys

1. INTRODUCTION

Galaxy-scale strong gravitational lenses represent a uniquely precise tool for measuring the mass density parameters of galaxies at cosmological distances, and their importance to the study of galaxy structure and evolution continues to increase as known examples become more numerous. Within this area, the method of spectroscopic gravitational lens selection stands out for its productivity and for its ability to deliver precise redshifts of both components in a lens system. In this method, lens systems are found through data mining procedures within large spectroscopic galaxy redshift survey databases that identify at least one emission-line (such as [O II] $\lambda 3727$) in a target galaxy's spectrum that originates from a more distant background source. In the context of spectroscopic lens surveys such as the Sloan Lens ACS Survey (SLACS: Bolton et al. 2006, 2008; Auger et al. 2009), the Optimal Line-of-sight Survey (OLS: Willis et al. 2005, 2006), the Sloan WFC Edge-on Late-type Lens Survey (SWELLS: Treu et al. 2011), the BOSS Emission-Line Lens Survey (BELLS: Brownstein et al. 2012), and possible similar studies within future projects such as BigBOSS (Schlegel et al. 2009), it has become imperative to understand the spectroscopic lens selection function, in order to draw accurate conclusions about the mass-density parameters of the parent population.

A detailed investigation of the selection function of spectroscopically discovered gravitational lenses was first made by Dobler et al. (2008). That work focused primarily on predicting the overall incidence of lenses within the Sloan Digital Sky Survey (SDSS: York et al. 2000) spectroscopic database from which the SLACS lenses were selected. Our current work is distinguished by the use of

a more accurate [O II] luminosity function, a focus on the *relative* incidence of lenses as a function of other physical parameters and the associated selection and modeling biases, and a consideration of the effects of variations in the radial gradient of the mass-density profile of the lens galaxies. Our goal is to quantify the parameter distribution biases of spectroscopic lens samples relative to the parent galaxy samples from which they are selected. In contrast to Dobler et al. (2008), we rely almost exclusively on Monte Carlo methods as opposed to analytic methods. Our current work is also complementary to the work of van de Ven et al. (2009) and Mandelbaum et al. (2009), which quantify the (much different) selection biases of lenses discovered within imaging survey data.

Our approach in this paper is to use controlled Monte Carlo simulations to generate mock lens and source catalogs with realistic parameters, to numerically analyze the magnification of these systems using ray-tracing techniques, then to apply SDSS-like spectroscopic selection cuts as well as modeling constraints to determine which mock lens and source parameters are preferentially selected and modelable as strong gravitational lens systems. Our aim is to allow the selection biases in spectroscopic galaxy-scale strong lens surveys to be understood and corrected, and to aid in the design of future surveys and follow-up observations.

This paper is structured as follows. We describe the Monte Carlo simulation method and generation of the mock catalogs in §2. In §3, we present the results of our simulations. We discuss these results and draw conclusions in §4. We assume a general-relativistic Friedmann-Robertson-Walker (FRW) cosmology with matter-density parameter $\Omega_m = 0.3$, vacuum energy-density parameter $\Omega_\Lambda = 0.7$, and Hubble parameter $H_0 = 70 \text{ km s}^{-1} \text{ Mpc}^{-1}$ throughout this paper. (Note however that our results are almost completely insensi-

tive to the detailed values of these cosmological parameters.)

2. MONTE CARLO SIMULATION

In this section we describe our Monte Carlo lens system simulation procedure in detail. An overview of the steps is as follows:

1. Generate a mock catalog of lens galaxy parameters,
2. Generate a mock catalog of source galaxy parameters,
3. Calculate the magnification of the source galaxy observed within a SDSS fiber,
4. Randomly select an [O II] luminosity for the source galaxy,
5. Calculate the [O II] line-flux in the fiber,
6. Determine if the source line-flux is detected,
7. Determine if the lens system is modelable.

These steps were repeated over a sequence of runs for two representative background source redshifts z_s and three representative mean Einstein radius values $\overline{\theta_E}$ described in further detail below. The first three steps define a particular lens geometry, and each run includes 1 million random realizations. Each of these realizations was associated with 1 million random draws from the luminosity function, leading to 10^{12} effective realizations per run. The simulations were carried out over several days of run time on a computer cluster with 8 nodes of 12 processor cores each.

2.1. Lens Galaxy Catalog

The singular power-law ellipsoid (SPLE) (Barkana 1998) was chosen as the parametric model for the mock lens galaxy catalog. The SPLE is a generalization of the singular isothermal ellipsoid (SIE) (Kassiola & Kovner 1993; Kormann et al. 1994; Keeton & Kochanek 1998) by means of an additional parameter, γ , which describes the mass density power-law index, where $\rho \propto r^{-\gamma}$. A power-law index of $\gamma = 2.0$ corresponds to a SIE model in the circular limit. A γ greater than (or less than) two corresponds to a steeper (or shallower) lensing potential.

The parameters we consider in the creation of our mock lens galaxy catalog included: the mass normalization of the lensing galaxy (i.e. the Einstein radius, θ_E), the power-law index γ of the mass density profile, and the projected mass axis ratio q . It is important to point out that although in this paper we use Einstein radius as a proxy for the mass of the lens galaxy it does not imply only circularly symmetric lens configurations or Einstein rings. In the limit of a singular isothermal sphere, the Einstein radius is related to the physical mass through

$$\theta_E = 4\pi \frac{\sigma_v^2}{c^2} \frac{D_{LS}}{D_S}, \quad (1)$$

where σ_v is the velocity dispersion of the lens galaxy, D_{LS} and D_S are cosmological angular-diameter distances from lens to observer and observer to source, respectively. Based on this relationship, θ_E can be considered as a stand-in for σ_v at fixed lens and source redshift. Following Shu et al. (2012) who find a typical RMS dispersion

of 0.075 dex in σ_v at fixed luminosity and redshift for massive galaxies at redshift $z \sim 0.5$, we adopt a log-normal Einstein radius distribution in our simulations with an intrinsic RMS dispersion of 0.15 dex. Since we randomly draw from a distribution in θ_E rather than σ_v , the simulation itself is independent of lens galaxy redshift. We explore the parameter space by considering log-normal distributions centered on Einstein radii of $\overline{\theta_E} = 0''.5$, $1''.0$, and $2''.0$ in separate simulations, thus spanning the representative range of galaxy-scale strong lensing systems. The mass density power-law indices of the SPLE lens galaxies are drawn from a Gaussian distribution, with $\gamma = 2.0 \pm 0.2$, further constrained to be between $1.0 \leq \gamma \leq 3.0$, throughout. We adopt this distribution as it is both representative of the SLACS lens galaxies (Koopmans et al. 2006) and capable of sampling parameter space. The mass axis ratios are drawn from a distribution which approximately replicates the results found in Holden et al. (2009, Figure 6) for the ellipticities of early-type galaxies from $z \sim 0$ to $z \sim 1$. The simulated lens galaxies are placed at the center of the simulated spectroscopic fiber aperture, and an intermediate axis convention is used for Einstein radius normalization of elliptical lens models. There is no need to randomly orient the position angle of the lenses, as the simulated source galaxies are randomly positioned.

2.2. Source Galaxy Catalog

In the creation of the mock source galaxy catalog we consider: the source scale radius, r_s , the position in the fiber, and the source redshift, z_s . The surface density profile of the source is assumed to be an exponential disk and the scale radii of the sources are assumed to be uniformly distributed between $0''.005 \leq r_s \leq 1''.0$. The lower limit is chosen to correspond to a source with a radius of half a pixel in the pixelized source plane of the simulation. Source positions are uniformly distributed within a circular region of radius 2.5 times the spectroscopic fiber radius centered on the lens in the source plane. A radius significantly larger than the fiber is necessary to obtain sufficient representation of unlensed sources at large radii that nevertheless contribute detectable line flux within the fiber. We represent SLACS-like systems by setting the source redshift to be $z_s = 0.6$, based on the source redshift distribution of 0.63 ± 0.20 found for the SLACS grade-A lenses. As our simulations are designed, the value of z_s only affects the detailed form of the source luminosity function (below) and the projection of the observational detection threshold within it.

2.3. System Catalog

In order to create simulated lens system, each of the lens galaxy parameters from the lens catalog were pairwise randomly associated with each of the parameters from the source galaxy catalog. This leads to a variety of lensed image configurations: doubles, three-image naked cusps, quads, rings, and of course a large number of singly-imaged sources.

2.4. Source Magnification

Here we summarize the method used to calculate the magnification of the source line-flux as seen through the spectroscopic fiber. In lens surveys such as SLACS (or BELLS), it is critical to account for the finite solid-angle of the original SDSS fiber of radius $1''.5$, or the

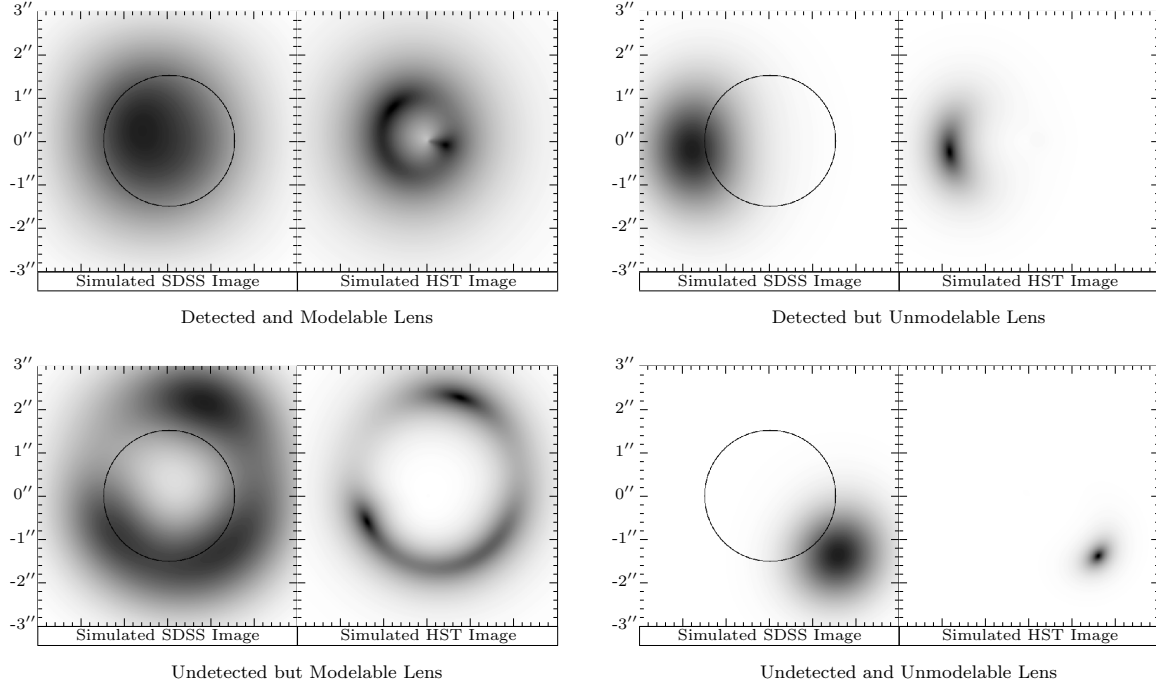


FIG. 1.— Example lens images from the mock SLACS simulations as would be seen by the SDSS (left) and Hubble Space Telescope (right). The circle represents a SDSS fiber ($3''$ in diameter). The seeing was taken to be $1''.5$ (FWHM) for the simulated SDSS images and $0''.05$ (FWHM) for the simulated HST images.

upgraded SDSS-III BOSS fiber of radius $1''.0$ (Eisenstein et al. 2011). The strength of the source emission-line is directly related to how much line-flux from the source galaxy is received into the fiber before it is sent to the spectrographs. If the lens galaxy has an Einstein radius larger than the radius of the fiber it is possible that no, or very little, source flux will be received by the fiber and the lens system will fail to be detected. This doesn't mean, however, that large Einstein radius lenses can't be spectroscopically detected. Seeing effects also need to be accounted for, especially because the seeing full-width half-maximum (FWHM) is as large (or larger than) the fiber radius. Seeing effects can either add flux to the fiber if the source image is outside the fiber or remove flux from the fiber if the source image is inside the fiber, as demonstrated in Figure 1.

The fiber magnification is defined to be

$$\mu_{fib} = \frac{f_r}{f_i}, \quad (2)$$

where f_r is the lensed source flux received by the fiber and f_i is the intrinsic (unlensed) source flux that would have been received in the absence of lensing and fiber effects. The lensed source flux f_r (in arbitrary units) received by the fiber is calculated by first generating a $8'' \times 8''$ (800^2 pixels) lensed image by ray-tracing the source plane image through the analytic lens mass model and subsequently integrating over a fiber mask convolved with the SDSS seeing PSF ($1''.5$ FWHM) centered on the lens galaxy. This second step is mathematically equivalent, and computationally faster, to convolving the lensed image with the seeing PSF and then applying the top-hat fiber mask. The intrinsic source flux f_i (in the same arbitrary units) is found by computing and integrating an unlensed image of the same parameterized source galaxy, and the scalar magnification μ_{fib} is given by the resulting ratio. The computation of simulated lensed images is the

most computationally intensive aspect of our procedure.

2.5. [O II] Luminosity & Line-Flux

The [O II] luminosity function for our simulations is interpolated between low redshifts, using the results of Gilbank et al. (2010), and redshifts $z \sim 1$, using the results of Zhu et al. (2009). In both papers, the [O II] luminosity function is fitted by a double power law:

$$\phi(L_{OII}, z_s) = \frac{dN}{dL_{OII}} \propto L_{OII}^{-\alpha}, \quad (3)$$

where L_{OII} is the [O II] luminosity and α is a dimensionless parameter. Thus, we interpolate the turnover luminosity (L_{TO}) in the power law function as well as the slopes at brighter (α_b) and fainter (α_f) luminosities from L_{TO} as a function of redshift. Each source galaxy in a particular lens configuration is assigned 10^6 randomly drawn [O II] luminosities according to the interpolated luminosity function, which in turn depends on the assumed source redshift. The [O II] luminosity functions for both source redshifts considered in this work are presented in Figure 2. Note that the source size and [O II] luminosity are assumed to be uncorrelated.

The simulated [O II] line-flux for each realization, S_{OII} , is given by the equation:

$$S_{OII} = \frac{L_{OII} \mu_{fib}}{4 \pi D_L^2}, \quad (4)$$

where L_{OII} is the [O II] luminosity, μ_{fib} is the fiber magnification, and D_L is the cosmological luminosity distance from observer to source. After calculating the line-flux received by a fiber, the detection classification of a realization is dependent on the delivered line flux relative to the noise limit of the SDSS spectroscopy. In order to determine this detection limit, the median and RMS 1σ line-flux for the SDSS spectroscopic database is calculated from $\sim 8 \times 10^5$ spectra from the SDSS seventh

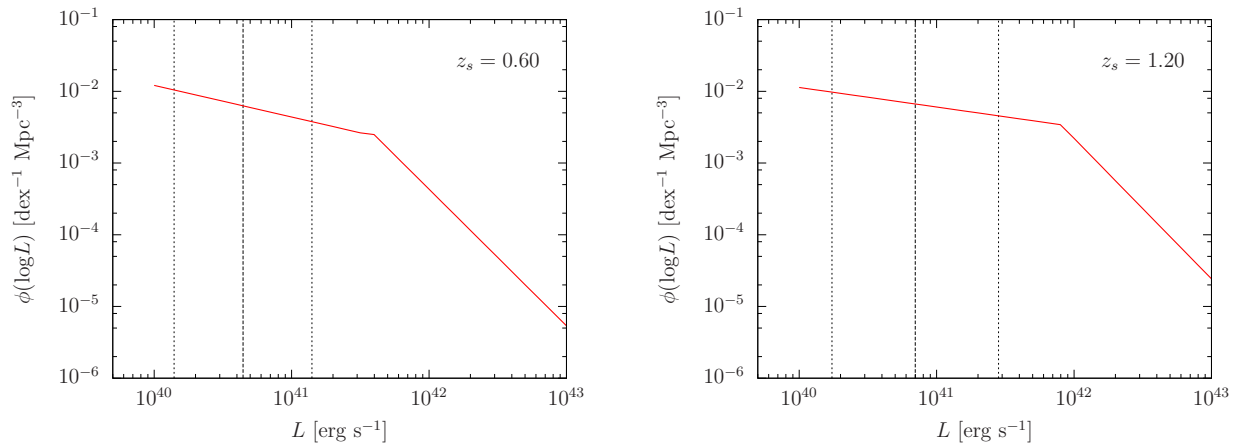


FIG. 2.— The [O II] luminosity functions (red) from which the source luminosities were drawn in the simulation. The left and right panels represent the luminosity function at $z_s = 0.60$ and $z_s = 1.2$, respectively. The lowest luminosity considered was 10^{40} erg s $^{-1}$. The dashed lines represent the calculated average source luminosity for each redshift, the dotted lines are the calculated 1σ deviations in those luminosities. The luminosity function at $z_s = 0.60$, $(\alpha_f, \alpha_b, \log L_{TO}) = (-1.46, -2.90, 41.50)$ and at $z_s = 1.2$, $(\alpha_f, \alpha_b, \log L_{TO}) = (-1.27, -2.96, 41.91)$.

data release (DR7) (SDSS collaboration: Abazajian et al. 2009). Figure 3 shows the median 1σ line-flux and RMS for SDSS. A 1σ line flux noise limit for the [O II] 3727 emission-line at the source redshift is drawn from this normal distribution for each realization. If the calculated [O II] 3727 line-flux of the catalog source is greater than six times this randomly drawn 1σ value, the simulated source is considered to be detected.

2.6. Modelable Constraints

The criteria used for determining the modelability of each lens system was estimated from the results of SLACS grade-A lens models. We consider a system to be “modelable” as a strong lens if its Einstein radius is greater than the minimum Einstein radius of the lenses modeled by Brownstein et al. (2012) and if the source position is within the radial caustic of the SIE lens model. Numerically, these requirements are that $\theta_E > 0''.5$ and that the source position is less than $2\theta_E$. This second limit corresponds to the point at which a counter-image of the source appears in the image plane in the case of a singular isothermal sphere (SIS), and encodes a requirement for multiple imaging in order to classify a system as a lens and to fit a strong-lens model. Although not all the lenses are SISs, this constraint is reasonably general. Note that a lens configuration is classified as either modelable or not depending upon its geometry, but independent of its [O II] line flux. For a given lens configuration, the multiple [O II] luminosity realizations allow us to compute a fractional detectability value. Lenses that are detected but not modelable correspond to “false positive” candidates, which nevertheless play an important role in the population distribution considerations to be discussed further below.

2.7. Mock BELLS Simulation

In order to extend the simulation and to understand the effects that survey-specific parameters have on the selection biases, we also run the simulation with parameters typical of the BELLS survey. We decrease the fiber radius to $1''.0$ to conform to the SDSS-III BOSS fiber upgrade (Eisenstein et al. 2011). To replicate the depth of the BELLS survey, from which 25 definite and 11 probable strong galaxy-galaxy lenses have been discov-

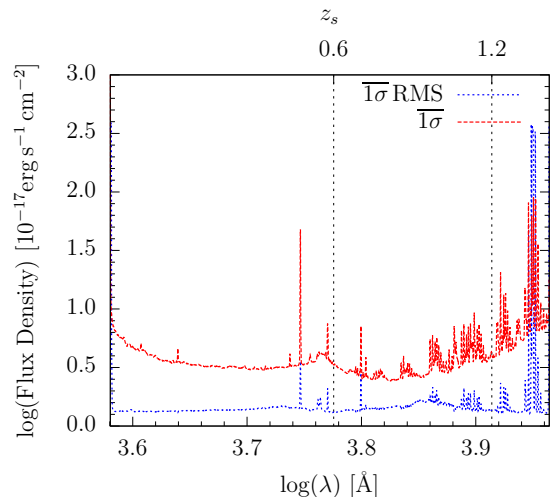


FIG. 3.— The log median 1σ [O II] line-flux, $\overline{1\sigma}$, detection limit spectrum for SDSS (dashed red) and the log [O II] 1σ RMS (dotted blue), each as a function of observed log [O II] wavelength, on the lower horizontal scale, and simulation redshifts, on the upper horizontal scale. The values were compiled from $\sim 8 \times 10^5$ spectra from the SDSS DR7. The dashed vertical lines show where the sources tested by the simulation lie within the noise spectrum.

ered with source redshifts, $z_s = 1.2 \pm 0.2$ (Brownstein et al. 2012), we place the sources at redshift of $z_s = 1.2$. Although a rigorous treatment of the mock BELLS simulation would recalculate the median 1σ [O II] line-flux of Figure 3 specifically for BOSS spectra, we leave this for future work; for our purposes here, we simply lower the detection criteria from 6σ to 4σ to mimic the anticipated fainter detection threshold of BOSS spectroscopy. Again we explore parameter space by considering the same mean Einstein radii of $\overline{\theta_E} = 0''.5, 1''.0$, and $2''.0$ for the parent distributions; all other parameter distributions were left unchanged.

2.8. Completeness Simulation

In addition to the simulations above, which aim to quantify parameter biases in lens samples selected from realistic lens and source distributions, we carry out two simulations with uniform input distributions in the Einstein radius θ_E and mass-density slope parameter γ , in

TABLE 1
MOCK SIMULATION PARAMETERS WITH DETECTED AND MODELABLE RESULTS

Run	z_s	Parent		Detected					Modelable				
		$\bar{\theta}_E$ ["]	$\sigma(\theta_E)$ [dex]	$\bar{\theta}_E$ ["]	$\sigma(\theta_E)$ [dex]	γ	Number	Percent	$\bar{\theta}_E$ ["]	$\sigma(\theta_E)$ [dex]	γ	Number	Percent
1	0.60	0.5	0.15	0.51	0.15	1.99 ± 0.20	8.42×10^3	0.84%	0.64	0.09	1.99 ± 0.20	3.59×10^3	42.61%
2	0.60	1.0	0.15	1.01	0.15	1.99 ± 0.20	9.06×10^3	0.91%	1.03	0.14	1.99 ± 0.20	8.39×10^3	92.67%
3	0.60	2.0	0.15	1.87	0.14	1.97 ± 0.20	7.74×10^3	0.77%	1.87	0.14	1.97 ± 0.20	7.70×10^3	99.54%
4	1.20	0.5	0.15	0.52	0.15	1.98 ± 0.20	1.85×10^3	0.19%	0.64	0.09	1.98 ± 0.20	9.60×10^2	51.86%
5	1.20	1.0	0.15	0.99	0.14	1.97 ± 0.20	2.05×10^3	0.20%	1.00	0.13	1.97 ± 0.20	1.97×10^3	96.42%
6	1.20	2.0	0.15	1.71	0.13	1.93 ± 0.20	1.24×10^3	0.12%	1.71	0.13	1.93 ± 0.20	1.24×10^3	99.89%

NOTE. — The Run number reflects the results found in Figure 4 with Runs 1–3 and Runs 4–6 corresponding to the mock SLACS and BELLS simulations, respectively. z_s represents the source redshift. The mean Einstein radii are given by $\bar{\theta}_E$ (and in fact represent exponentiated mean log Einstein radii). The standard deviation of the Einstein radii, $\sigma(\theta_E)$, are in units of dex. The values of $\bar{\theta}_E$ and $\sigma(\theta_E)$ presented for the Parent sample are the input values upon which the distributions are drawn. All of the Parent samples had mass density power-law index, γ , distributions with a mean of 2.0 and a standard deviation of 0.2. The values of $\bar{\theta}_E$, $\sigma(\theta_E)$, and γ for the detected and modelable lenses were calculated by fitting a gaussian function to the binned histograms. Each run included 10^6 mock lens systems in the Parent samples. The “Number” columns indicate the number of mock lens systems generated by the Monte Carlo simulation which were detected, and the “Number” determined to be modelable. The “Percent” of detected lenses is relative to the Parent sample of 10^6 systems, whereas the “Percent” of modelable lenses is relative to the Detected sample.

order to assess spectroscopic selection completeness in the plane spanned by these two parameters. We compute 2×10^6 realization for both SLACS-like and BELLS-like parameters, and quantify both the detected and detected+modelable fractions as a function of these parameters.

3. RESULTS

In this section we present the results of the Monte Carlo simulation, outlined in §2, used to generate 1×10^6 lens systems per run. The results for each run are summarized in Table 1. Figure 4 depicts the histograms of the Einstein radius, lens mass density power-law index, lens mass axis ratio, and effective source size for the parent, detected, and modelable lenses for each of the runs. Note that by “modelable” we are referring to the modelable subset of *detected* systems (since this is the experimentally relevant definition), even though it is possible for an undetected system to be modelable in its geometry. As suggested by the procedure discussed in §2, the lens selection biases can be divided into a detection bias and a modeling bias. Throughout this section both biases will be presented side-by-side with respect to a given parameter. We first discuss the results of the SLACS-like simulations.

3.1. Dependence on Lens Parameters

The mean Einstein radius (or rather, the exponentiated mean log Einstein radius) and standard deviation for the detected and modelable samples were calculated by fitting a Gaussian function to the binned histograms displayed in Figure 4. The only appreciable bias in detected $\bar{\theta}_E$ shows up for the simulated population with a mean $\bar{\theta}_E = 2''.0$, due to the finite size of the fiber. As the Einstein radius or strength of the lens increases the chance that enough of the lensed image falls inside the fiber to be detected decreases. And, as mentioned in §2.4, even though the seeing effects may introduce more flux into the fiber for images outside the fiber it simply may not be enough for the system to be detected. The only hope for a large Einstein radius lens to be detected is if it has a bright counter-image that lies within the fiber, which is possible but not probable. The fiber still imparts a bias against large separation lenses. The bias

in Einstein radius for the modelable lenses, by contrast, is most appreciable for parent samples with the small mean Einstein radius of $\bar{\theta}_E = 0''.5$. This results from the requirement that $\theta_E \geq 0''.5$, which eliminates small radius lenses and increases the average modelable Einstein radius.

The overall percentage of detected systems is small—less than 1%—and is maximized for the parent sample with mean Einstein radius $\bar{\theta}_E = 1''.0$. The overall percentage of modelable lenses increase as the parent-sample mean Einstein radius is increased, from $\sim 43\%$ when $\bar{\theta}_E = 0''.5$ to $\sim 99\%$ when $\bar{\theta}_E = 2''.0$. This is not surprising because the samples with greater mean Einstein radii have fewer lenses that fail to pass the modelable constraints.

The distribution in mass density power-law index of the detected and modelable samples reported in Table 1 were calculated by fitting a Gaussian function to the binned histograms shown in Figure 4. The bias in the lens power-law index relative to the parent sample is small, shifted towards slightly shallower lensing potentials in all simulation runs. This slight bias is introduced by the detection process; the modelable constraints introduced no additional bias. Furthermore, as the mean Einstein radius of the parent sample was increases, there is a slight but definite trend in the detected and modelable γ bias toward shallower potentials. This relation is further discussed in §3.5. The SLACS-like lens sample bias in γ is small enough (0.01 to 0.03) that it is probably negligible compared to other sources of uncertainty.

Finally, we note that for every run of the simulation there is no obvious bias in the lens mass axis ratio, either in terms of detectability or modelability. A similar result was found by Dobler et al. (2008).

3.2. Dependence on Source Parameters

Although we don’t quantify the detection and modelable biases for the source parameters, it is of interest to understand them qualitatively. As seen in Figure 4 there is a distinct bias towards smaller source sizes in both the detected and modelable samples in all of the SLACS simulations tested (runs 1–3). This result is likely attributed to the higher magnification small source sizes can acquire relative to larger source sizes which makes

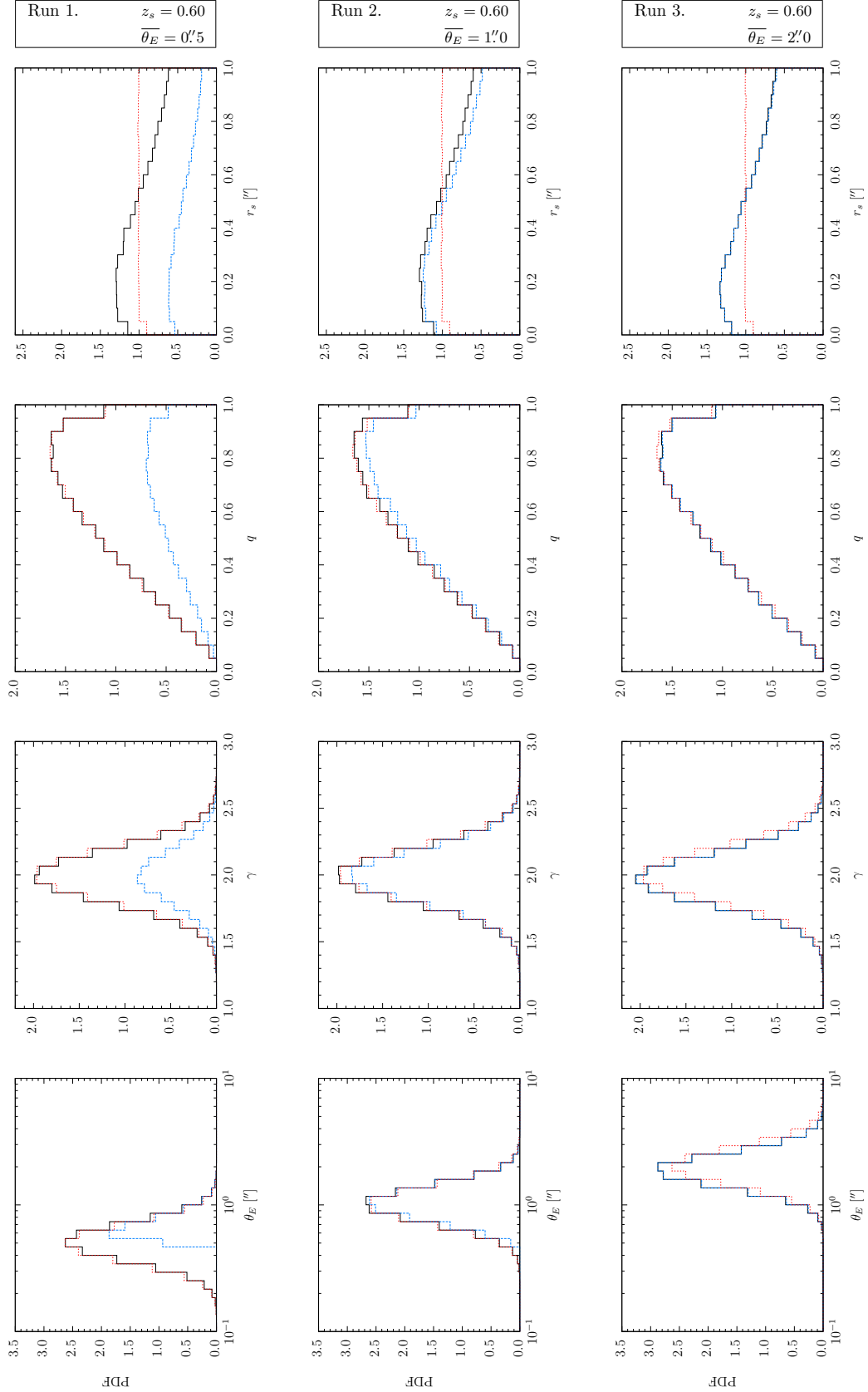


FIG. 4.— Einstein radius (θ_E), lens mass density power-law index (γ), lens mass axis ratio (q), and effective source scale radius (r_s) of the parent (dashed red line), detected (black line), and modelable (dashed blue line) lens samples for each run of the simulation, as summarized in Table 1, arranged by source redshift. From the top to bottom row, we vary the parent mean Einstein radius, $\overline{\theta_E}$, between $0''.5$, $1''.0$, and $2''.0$ respectively. The parent sample consisted of 1×10^6 mock lenses. The parent and detected histograms are normalized to unit area, whereas the modelable histogram is normalized to the fraction of modelable lenses relative to detected lenses.

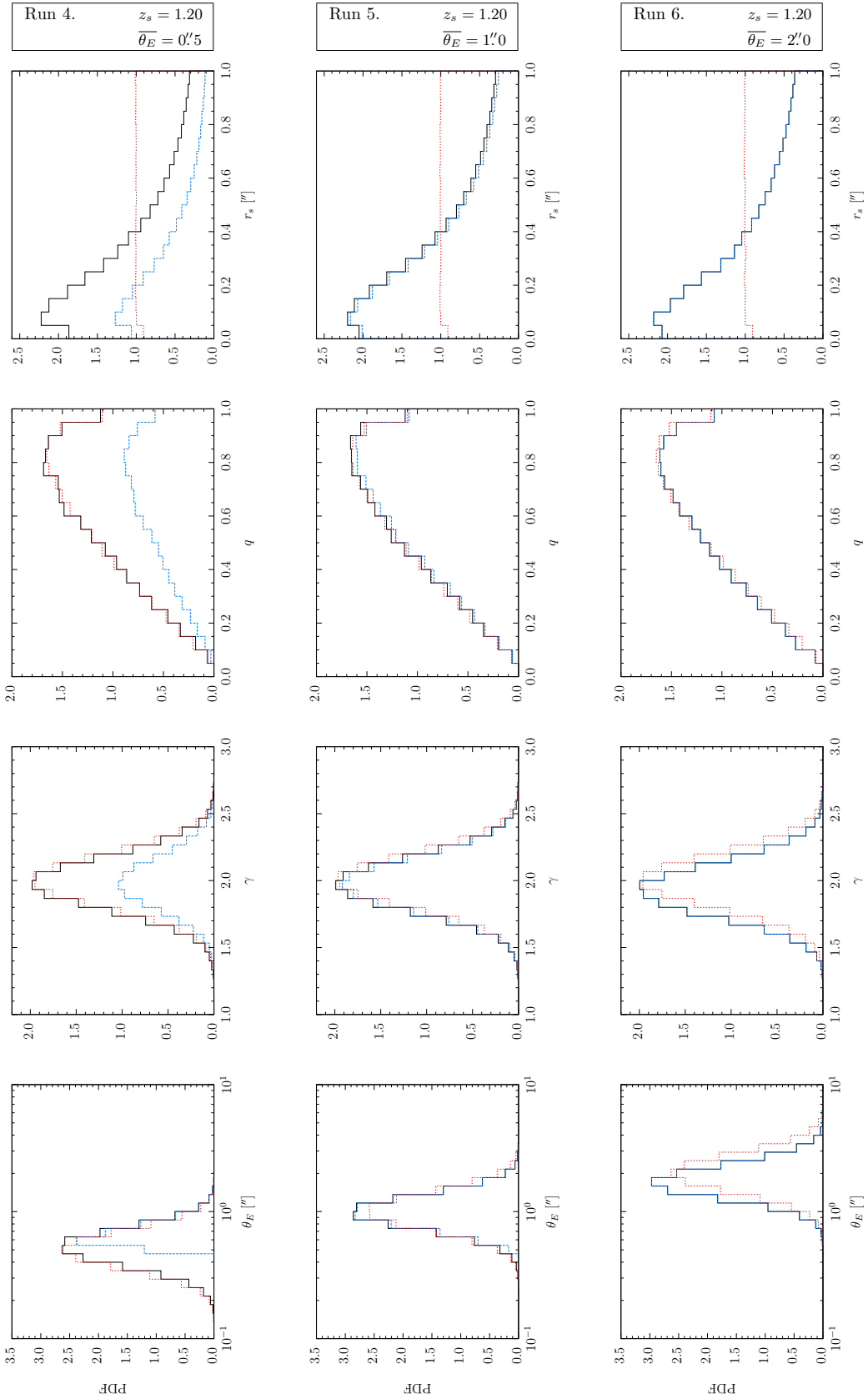


FIG. 4.— Continued.

them more likely to be detected. For every simulation tested, there is no detection or modelability bias in the source position.

3.3. Simulation Images

Figure 1 depicts example lens images from the mock SLACS simulations. It also illustrates the effects seeing has on the detection of lens systems. As seen in Figure 1 our simulation includes false positive lenses, or lenses which are detected but not modelable because they lack a counter-image. Of course our simulation also includes the opposite, lenses which are not detected but are modelable. These lenses fail to be detected either due to seeing effects, low source luminosity, or the lens images falling outside of the fiber. It is possible, however, for a system with a large Einstein radius and low mass density power-law index to be detected and subsequently classified as modelable when just the central, de-magnified image is inside the fiber. This is seen particularly at small source redshifts and high source luminosities. This effect makes the relationship between θ_E and γ an interesting one to investigate which we pursue in §3.5. Figure 1 also includes examples from the simulation which are detected and modelable as well as not detected and not modelable.

3.4. Mock BELLS Simulation Results

The results of runs 4–6 of the simulation with parameters typical of BELLS are displayed in the last three rows of Table 1 and Figure 4. One of the main differences between BELLS and SLACS is the size of the fiber, which we have already seen is an important selection effect and source of bias in spectroscopic strong lens surveys. This is manifested primarily in a more pronounced bias towards smaller detected Einstein radii and slightly shallower detected mass-density profiles for the simulation with the largest mean Einstein radius of $\overline{\theta_E} = 2''.0$. For the parent samples with smaller mean Einstein radii, the biases in γ remain small for both detected and modelable subsets, and the bias in $\overline{\theta_E}$ is small for the detected subsample. The modelable bias in $\overline{\theta_E}$ is zero for the $\overline{\theta_E} = 1''.0$ BELLS simulation, and is identical to bias in the SLACS simulation for the $\overline{\theta_E} = 0''.5$ parent sample. Another result of the BELLS simulation is that the percent of detected lenses is lower than the percent detected by any of the SLACS simulations. However, the average percent of modelable lenses is slightly higher than in the SLACS simulations. Compared to the SLACS simulations, the BELLS simulations also show a much more distinct bias in detecting smaller source sizes (see Fig. 4). Again as with the SLACS-like simulations, there is no bias in the lens mass axis ratio, detected or modelable.

3.5. Parameter Correlation

The results of our uniform exploration of the plane of θ_E and γ are presented in Figure 5. For both the detected and modelable lenses, as the Einstein radius increases the minimum detectable power-law index decreases monotonically. This effect is at least partially due to selection effects of spectroscopic surveys (i.e., the finite size of the fiber) which eliminate large separation lenses. In spite of this, the result implies that large radius, shallow lensing potentials could in principle be detected and modeled by spectroscopic surveys, but that such surveys are blind to large radius, steep lensing potential galaxies. However,

real systems with very large Einstein radii will tend to be of the group or cluster scale (exceeding 400 km s^{-1}), and will have more complicated lensing potentials: it is unclear whether our simple power-law model is applicable to such systems.

4. CONCLUSIONS

We have presented a simple Monte Carlo simulation used to explore the selection biases of spectroscopic strong galaxy-galaxy gravitational lens surveys. As Dobler et al. (2008) found and we confirm in this work, the size of the spectroscopic fiber is the most significant selection effect in strong galaxy surveys. *Detection* biases become important for parent populations with a mean Einstein radius of approximately $2''.0$, shifting the detected samples toward relatively smaller Einstein radii and shallower lensing potentials. *Modelability* biases become important for parent populations with smaller mean Einstein radii (of approximately $0''.5$), pushing the modelable subsamples to larger mean Einstein radii but not biasing the average mass-density profile significantly. We find that a majority of detected lenses are classified as modelable in all the simulations tested, thus explaining the efficiency of follow-up high-resolution imaging of spectroscopically discovered lens candidates. We find no significant bias in the lens mass axis ratio relative to the parent population.

An important implication of this work is that, for galaxy-scale spectroscopically selected lenses, the bias in the detected and modelable mass-density profile slope relative to the parent population is relatively small, and hence is not likely to be a major factor in the interpretation of results on the mass-density profile of lensing galaxies such as those of (Koopmans et al. 2006, 2009) and Bolton et al. (2012). However, the constraint of lens modelability for populations of lower mean Einstein radius indicates that the lenses selected from these populations are biased systematically towards higher velocity dispersions. One mitigating strategy to correct for this bias would be to include constraints from *non-lenses* along with constraints from lenses in the analysis of survey samples, since non-lenses with identifiable single-source images place upper limits on the velocity dispersions of their foreground galaxies.

The comparison between SLACS-like and BELLS-like simulations shows that the detailed parameters of the spectroscopic survey are important to determining the relevant details of the spectroscopic lens selection function. Nevertheless, there is significant commonality in the trends of selection bias between these two survey configurations. In view of the substantially uniform detection sensitivity of both SLACS-like and BELLS-like surveys across a broad range of Einstein radii and mass-density profile slopes, such surveys can be used to select representative samples of field galaxies for study through gravitational lensing, with biases that can be quantified and corrected. At group and cluster lens-mass scales, spectroscopic selection becomes much less efficient and also much more sensitive to the parameters of the mass-density profile.

The bias of spectroscopically selected lenses towards sources of smaller physical size, seen for both SLACS and BELLS simulations (with much greater magnitude in the latter) has important implications for the study of the lensed galaxy population discovered in these surveys. This effect can explain the mass-size offset seen in

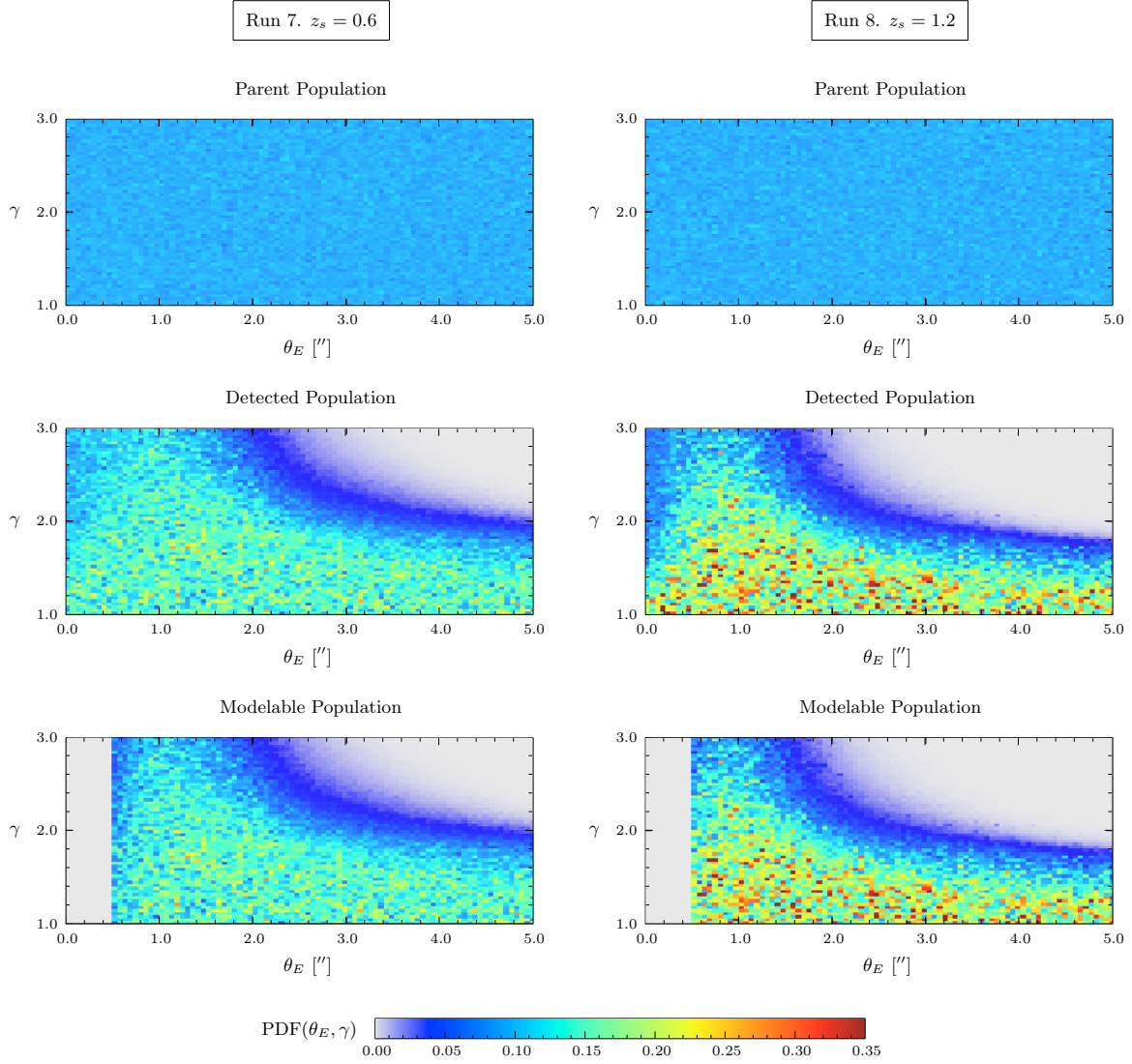


FIG. 5.— 2D histogram of the correlation between the lens mass density power-law index, γ , and lens Einstein radius, θ_E . The left panels correspond to mock SLACS simulations, with $z_s = 0.6$, and the right panels correspond to mock BELLS simulations, with $z_s = 1.2$. The top graphs show the parent samples of 2×10^6 lenses uniformly distributed across the shown ranges. The middle graphs show the distribution of the detected lenses, and the bottom graph shows the modelable lens sample distribution. The parent and detected histograms are normalized to unit area, whereas the modelable histogram is normalized to the fraction of modelable lenses relative to detected lenses. Notice the decrease in detected and modelable lenses with high mass density power-law indices at large Einstein radii and the cutoff in the modelable lens sample at low Einstein radii due to the modelable criteria.

the work of [Newton et al. \(2011\)](#) for lensed emission-line galaxies relative to broadband-selected unlensed galaxies at comparable magnitudes and redshifts. This bias of course affords the advantage of studying a systematically smaller and fainter population of galaxies than would be accessible without the strong lensing effect.

This work has highlighted the salient features of the selection function of spectroscopic gravitational lens surveys. Quantitative correction for the biases identified by this work will require simulations that account for varying source-galaxy redshifts and for multiple parent Einstein radius (i.e., velocity-dispersion) distributions. In future work we will integrate detailed implementations of our Monte Carlo simulations into the analysis of population distribution parameters for the combined SLACS and BELLS gravitational lens data set, thus allowing a more robust generalization from the physical nature of spectroscopic lens samples to the population of early-type field galaxies as a whole.

Funding for the SDSS and SDSS-II has been provided by the Alfred P. Sloan Foundation, the Participating Institutions, the National Science Foundation, the U.S. Department of Energy, the National Aeronautics and Space Administration, the Japanese Monbukagakusho, the Max Planck Society, and the Higher Education Funding Council for England. The SDSS Web Site is <http://www.sdss.org/>.

The SDSS is managed by the Astrophysical Research Consortium for the Participating Institutions. The Participating Institutions are the American Museum of Natural History, Astrophysical Institute Potsdam, University of Basel, University of Cambridge, Case Western Reserve University, University of Chicago, Drexel University, Fermilab, the Institute for Advanced Study, the Japan Participation Group, Johns Hopkins University, the Joint Institute for Nuclear Astrophysics, the Kavli Institute for Particle Astrophysics and Cosmology, the Korean Scientist Group, the Chinese Academy of Sciences (LAMOST), Los Alamos National Laboratory, the

Max-Planck-Institute for Astronomy (MPIA), the Max-Planck-Institute for Astrophysics (MPA), New Mexico State University, Ohio State University, University of

Pittsburgh, University of Portsmouth, Princeton University, the United States Naval Observatory, and the University of Washington.

REFERENCES

- Auger, M. W., Treu, T., Bolton, A. S., Gavazzi, R., Koopmans, L. V. E., Marshall, P. J., Bundy, K., & Moustakas, L. A. 2009, *ApJ*, 705, 1099, [arXiv:0911.2471](#)
- Barkana, R. 1998, *ApJ*, 502, 531, [arXiv:astro-ph/9802002](#)
- Bolton, A. S., Burles, S., Koopmans, L. V. E., Treu, T., Gavazzi, R., Moustakas, L. A., Wayth, R., & Schlegel, D. J. 2008, *ApJ*, 682, 964, [arXiv:0805.1931](#)
- Bolton, A. S., Burles, S., Koopmans, L. V. E., Treu, T., & Moustakas, L. A. 2006, *ApJ*, 638, 703, [arXiv:astro-ph/0511453](#)
- Bolton, A. S., et al. 2012, *ArXiv e-prints* (ApJL, submitted), [arXiv:1201.2988](#)
- Brownstein, J. R., et al. 2012, *ApJ*, 744, 41, [arXiv:1112.3683](#)
- Dobler, G., Keeton, C. R., Bolton, A. S., & Burles, S. 2008, *ApJ*, 685, 57, [arXiv:0803.2234](#)
- Eisenstein, D. J. et al. 2011, *AJ*, 142, 72, [arXiv:1101.1529](#)
- Gilbank, D. G., Baldry, I. K., Balogh, M. L., Glazebrook, K., & Bower, R. G. 2010, *MNRAS*, 405, 2594, [arXiv:1002.3172](#)
- Holden, B. P. et al. 2009, *ApJ*, 693, 617, [arXiv:0811.1986](#)
- Kassiola, A., & Kovner, I. 1993, *ApJ*, 417, 450
- Keeton, C. R., & Kochanek, C. S. 1998, *ApJ*, 495, 157, [arXiv:astro-ph/9705194](#)
- Koopmans, L. V. E., Treu, T., Bolton, A. S., Burles, S., & Moustakas, L. A. 2006, *ApJ*, 649, 599, [arXiv:astro-ph/0601628](#)
- Koopmans, L. V. E., et al. 2009, *ApJ*, 703, L51, [arXiv:0906.1349](#)
- Kormann, R., Schneider, P., & Bartelmann, M. 1994, *A&A*, 284, 285
- Mandelbaum, R., van de Ven, G., & Keeton, C. R. 2009, *MNRAS*, 398, 635, [arXiv:0808.2497](#)
- Newton, E. R., et al. 2011, *ApJ*, 734, 104, [arXiv:1104.2608](#)
- Schlegel, D. J., et al. 2009, [arXiv:0904.0468](#)
- SDSS collaboration: Abazajian, K. N. et al. 2009, *ApJS*, 182, 543, [arXiv:0812.0649](#)
- Shu, Y., et al. 2012, *AJ*, in press, [arXiv:1109.6678](#)
- Treu, T., et al. 2011, *MNRAS*, 417, 1601, [arXiv:1104.5663](#)
- van de Ven, G., Mandelbaum, R., & Keeton, C. R. 2009, *MNRAS*, 398, 607, [arXiv:0808.2493](#)
- Willis, J. P., Hewett, P. C., & Warren, S. J. 2005, *MNRAS*, 363, 1369, [arXiv:astro-ph/0508430](#)
- Willis, J. P., Hewett, P. C., Warren, S. J., Dye, S., & Maddox, N. 2006, *MNRAS*, 369, 1521, [arXiv:astro-ph/0603421](#)
- York, D. G., et al. 2000, *AJ*, 120, 1579, [arXiv:astro-ph/0006396](#)
- Zhu, G., Moustakas, J., & Blanton, M. R. 2009, *ApJ*, 701, 86, [arXiv:0811.3035](#)